



UNIVERSITY OF LEEDS

This is a repository copy of *Towards automated design of quantum cascade lasers* .

White Rose Research Online URL for this paper:

<http://eprints.whiterose.ac.uk/1692/>

Article:

Mircetic, A., Indjin, D., Ikonc, Z. et al. (3 more authors) (2005) Towards automated design of quantum cascade lasers. *Journal of Applied Physics*, 97 (8). 084506-(7 pages). ISSN 1089-7550

<https://doi.org/10.1063/1.1882768>

Reuse

See Attached

Takedown

If you consider content in White Rose Research Online to be in breach of UK law, please notify us by emailing eprints@whiterose.ac.uk including the URL of the record and the reason for the withdrawal request.



eprints@whiterose.ac.uk
<https://eprints.whiterose.ac.uk/>

Towards automated design of quantum cascade lasers

Aleksandra Mirčetić

Faculty of Electrical Engineering, P.O. Box 35-54, 11120 Belgrade, Serbia and Montenegro

Dragan Indjin, Zoran Ikonić, and Paul Harrison

School of Electronic and Electrical Engineering, University of Leeds, Leeds LS2 9JT, United Kingdom

Vitomir Milanović

*Faculty of Electrical Engineering, P.O. Box 35-54, 11120 Belgrade, Serbia and Montenegro
and School of Electronic and Electrical Engineering, University of Leeds, Leeds LS2 9JT, United Kingdom*

Robert W. Kelsall

School of Electronic and Electrical Engineering, University of Leeds, Leeds LS2 9JT, United Kingdom

(Received 12 October 2004; accepted 3 February 2005; published online 12 April 2005)

We present an advanced technique for the design and optimization of GaAs/AlGaAs quantum cascade laser structures. It is based on the implementation of the simulated annealing algorithm with the purpose of determining a set of design parameters that satisfy predefined conditions, leading to an enhancement of the device output characteristics. Two important design aspects have been addressed: improved thermal behavior, achieved by the use of higher conduction band offset materials, and a more efficient extraction mechanism, realized via a ladder of three lower laser states, with subsequent pairs separated by the optical phonon energy. A detailed analysis of performance of the obtained structures is carried out within a full self-consistent rate equations model of the carrier dynamics. The latter uses wave functions calculated by the transfer matrix method, and evaluates all relevant carrier-phonon and carrier-carrier scattering rates from each quantized state to all others within the same and neighboring periods of the cascade. These values are then used to form a set of rate equations for the carrier density in each state, enabling further calculation of the current density and gain as a function of the applied field and temperature. This paper addresses the application of the described procedure to the design of $\lambda \sim 9 \mu\text{m}$ GaAs-based mid-infrared quantum cascade lasers and presents the output characteristics of some of the designed optimized structures. © 2005 American Institute of Physics. [DOI: 10.1063/1.1882768]

I. INTRODUCTION

Quantum cascade lasers (QCLs) pioneered by the Lucent group¹ are sophisticated infrared light sources with emission wavelengths that can be tuned by engineering the electronic energy states and wave functions.²⁻⁷ This is enabled by their complex structure, in which the sequence of alternating layers of different semiconductor materials is repeated many times. The first QCLs have been realized in the InGaAs/AlInAs system, lattice matched on InP, and a significant improvement of the device performance, such as broad-band emission⁸ or continuous wave room temperature⁹ and ultrahigh power operation¹⁰ has been achieved since. On the other hand, the GaAs/AlGaAs system offers more growth flexibility, and since the first QCL realization⁵ an impressive extension of the emission wavelength range from mid-infrared to terahertz^{11,12} has been demonstrated. Several mid-infrared GaAs-based QCL have achieved pulsed room temperature operation.¹³⁻¹⁷ However, the output characteristics of these devices are still poor in comparison to InP based mid-infrared QCLs, demanding further optimization of layer structures and investigations of the influences of relevant physical and technological parameters.^{18,19} As the GaAs/AlGaAs system is lattice matched, the alloy composition and layer width can be varied independently. In mid-infrared devices, the separations between the energy states in

the active region are set by the desired emission wavelength (between the active laser levels) and the longitudinal optical (LO) phonon energy (between the ground and lower laser level), which facilitates the population inversion by allowing the fast emptying of the lower laser state by means of non-radiative transitions. However, parameters of interest in the calculation of the optical gain, such as the population inversion and the transition matrix element, still depend, via the wave functions, on the potential profile which may be varied to optimize performance of the structure. The relationships between these parameters are very complex, making the optimization process difficult and demanding.²⁰⁻²² A large spatial overlap between the electronic wave functions of the lasing states increases the dipole matrix element which enhances the optical transition, but also results in the reduction of the electron-longitudinal optical phonon scattering time. Since these two parameters influence the gain in an opposite manner, a balance has to be found to ensure the proper operation of a QCL, and it becomes apparent that an appropriate optimization technique should be employed.

A prerequisite for the design of QCL structures is the existence of a systematic and precise modeling technique which would provide a deeper insight of the physical processes that occur in these complex devices, and, at the same time, enable the improvement of existing structures. The charge transport through a quantum cascade laser is thought

to be mainly caused by incoherent electron–longitudinal optical phonon (LO) and electron–electron scattering,²³ and the inclusion of all mechanisms that take place in both the active and injector/collector regions of the structure is essential for an accurate description of the carrier dynamics. This is particularly significant in view of the fact that the gain values calculated from the simple three-level model under the unity injection approximation considerably depart from those obtained experimentally,^{24–27} which is believed to be due to thermal activation of carriers directly into the continuum^{13,28} and cannot be described within a simple model. The existence of this parasitic current path is one of the main obstacles in extending the working temperature range of GaAs-based QCLs. In order to suppress the parasitic currents it is necessary to lower the active region levels deeper into the multi-quantum-well potential, which can be achieved by either increasing the operating wavelength or by using a higher conduction band offset.

In the work presented here, we have addressed the optimization of 9 μm GaAs QCLs, starting from the structure described in Refs. 13–15. Two types of active regions with appropriate injectors/collectors are developed, with the intention of focusing on two important design features: improved temperature behavior and a more efficient extraction mechanism. The first structure comprises a step triple-quantum (TQW) system and is characterized by vertical transitions which occur in the active region, while the second one relies on a ladder of three lower laser states, separated by optical phonon energy, resulting in a decrease of the lower laser level population. The Al content in the barriers of both structures is taken to be 45%, which compared to the standard 33% Al content, should give an increase of the band offset of about¹³ 95 meV. In addition, the continuum levels in both structures are positioned approximately 50 meV above the upper laser level, leading to reduced parasitic currents. The output characteristics of these structures are then evaluated using the full self-consistent rate equation model.^{24,25} The results of the calculations performed for the existing structure show excellent agreement with the experimentally obtained values^{13–15} and, at the same time, a noticeable improvement is predicted for the optimized QCLs.

II. THEORETICAL CONSIDERATIONS

A. The implementation of the simulated annealing algorithm

In this work, we have used a global iterative procedure implemented within a modification of the continuous simulated annealing (SA) algorithm developed by Goffe, Ferrier, and Rogers.^{29,30} It searches for the global optimum of an N -dimensional target function F , where N represents the number of optimization variables. The step length is controlled by a parameter called “temperature.” As the optimization process proceeds and the “temperature” drops, the step length declines and the algorithm closes in on the global optimum. The “temperature” drop is controlled by a parameter called the “temperature reduction factor,” RT , as $T(i+1) = RT \times T(i)$, where i represents the iteration counter. The value of this parameter, suggested by the authors of the

algorithm,²⁹ is 0.85. Before the “temperature” is changed, the algorithm performs $NT \times NS \times N$ function evaluations, where NS and NT are user supplied variables, with suggested values of 20 and $\max(100, 5N)$, respectively.²⁹

SA can easily be adapted for the needs of quantum heterostructure design. The N variables that define the parameter space are physical device parameters, such as the layer thicknesses, potential barrier heights, applied bias, etc. The parameter vector, whose entries correspond to the physical variables that are to be optimized, is defined. The performance of a structure is described by formulating an objective function. It includes performance variables, such as transition matrix elements or scattering times, which depend on the physical parameters vector. The algorithm then finds the global optimum of the objective function in the N -dimensional parameter space and determines the physical parameters vector which produces a system as close as possible to the ideal one.

Simulated annealing was adopted as the optimization algorithm of choice for a variety of reasons: it is mostly independent on the starting values, often a critical point in conventional optimization algorithms,²⁰ and it makes less strict assumptions about the candidate function, so it even need not be continuous. Also, it is possible to restrict the optimization to a subset of the parameter space to incorporate fabrication constraints. All of the above make this algorithm far more flexible than other techniques used for QCL characteristics optimization (for instance, the SUSYQM method³¹ which produces a smooth optimized potential profile that needs to be realized via further discretization).

Since the optimization of the entire QCL structure would be extremely computationally demanding, the optimization of the active region is carried out separately and, in the next step, a properly designed injector/collector is added. For the same reason, the state energies and wave functions needed for the objective function calculations are obtained by the shooting method which, while slightly less precise, demands significantly less computation time.

1. Active region optimization

The form of the optimization target function differs slightly depending on the active region shape. In the case of the triple step-quantum-well active region this is chosen so to enable the selection of potential profiles which would facilitate vertical transitions (VT) by increasing the influence of the transition matrix element on the objective function value. Vertical transition QCLs are characterized by a strong independence of wavelength on the applied field, which is a consequence of the collocation of the wave functions directly involved in the laser action, at the same time resulting in a large optical dipole matrix element and shorter electron scattering times. According to the three-level QCL model.^{2,32} (3-is the upper laser level, 2-is the lower laser level, and 1-is the ground level in the QCL active region) with assumed unity injection efficiency, the optimization function can be defined as the gain coefficient, given as

$$F = (1 - \tau_{21}/\tau_{32}) \cdot \tau_3 \cdot z_{32}^2, \quad (1)$$

where τ_{21} and τ_{32} are the scattering times, τ_3 the upper laser level lifetime, and z_{32} the dipole matrix element for the lasing transition.

The target is to maximize the objective function [Eq. (1)] without altering the transition energies ΔE_{21} and ΔE_{32} (defined by the LO phonon and transition energy, respectively) by more than a few meV, and keeping the fourth level positioned at least 50 meV above the upper laser level. While maintaining the energy differences, the shape of the wave functions can be modified by varying the potential profile in order to influence the parameters of interest in the calculation of the target function.

The parameter vector consists of eleven layer thicknesses d_i , $i=1, \dots, 11$, and the Al content in the steps as the twelfth parameter. Layer thicknesses are only allowed to have an integer number of crystalline monolayers, and must be positive or zero. Their widths are limited to 30 Å for steps and wells and 20 Å for barriers. The Al content in the steps is restricted as well, for the purpose of fabrication feasibility, and is allowed to acquire five different values: 0%, 11.25%, 22.5%, 33.75%, and 45%, where the upper bound is placed in order to retain direct band gap operation.

The optimization of a four-quantum well (4QW) active region is quite similar except for the number of optimization variables and the form of the objective function. The number of active region layers (and therefore the parameters that are to be optimized) is reduced to seven, resulting in a considerably shorter time needed to perform the calculation. However, the additional active region level implies an extra condition regarding the energy separations, since it is to be placed approximately 36 meV above the first excited active region state. The objective function is evaluated by solving a simplified rate equation system in which only levels localized in the active region are taken into account, while the injector/collector regions are considered within the unity injection/extraction efficiency approximation:

$$F = (1 - \tau_3/\tau_{43}) \cdot \tau_4 \cdot z_{43}^2. \quad (2)$$

For optimization purposes only, the required scattering times are simplified, and are determined by considering only the most dominant process in the active region—the electron–LO phonon scattering.

By carrying out “trial runs” of the optimization algorithm for different types of objective functions, we have found that the optimization function, as given in Eq. (2), encourages the selection of potential profiles that maximize the objective function mostly by increasing the upper laser level lifetime. This type of potential, where the upper and lower laser state wave functions are located in spatially different regions, supports diagonal transitions which result in smaller dipole matrix elements but longer carrier lifetimes.

2. Injector/collector region optimization

In the next step, a five QW injector region is created starting with the existing injector design described in Ref. 13. The chosen optimization function should, as closely as possible, represent the cascading fast relaxation of electrons

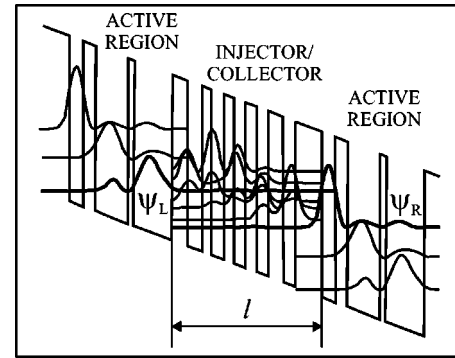


FIG. 1. A schematic diagram of one and a half QCL period with relevant left ψ_L and right ψ_R active region, and injector wave functions. l represents the injector/collector length.

down the staircase of injector energy levels which largely occurs via electron–electron scatterings. This is favored by good overlap of the wave functions and, considering the injector region with its two adjacent active regions, as given in Fig. 1, we propose this function to be written in terms of overlap factors, defined as

$$O^{(1)} = \sum_i \frac{O_{L,i} \cdot O_{i,R}}{|\Delta E_{L,i}| \cdot |\Delta E_{i,R}|}, \quad (3)$$

$$O^{(2)} = \sum_i \sum_{j \neq i} \frac{O_{L,i} \cdot O_{i,j} \cdot O_{j,R}}{|\Delta E_{L,i}| \cdot |\Delta E_{i,j}| \cdot |\Delta E_{j,R}|}, \quad (4)$$

$$O^{(3)} = \sum_i \sum_{j \neq i} \sum_{k \neq i,j} \frac{O_{L,i} \cdot O_{i,j} \cdot O_{j,k} \cdot O_{k,R}}{|\Delta E_{L,i}| \cdot |\Delta E_{i,j}| \cdot |\Delta E_{j,k}| \cdot |\Delta E_{k,R}|}, \quad (5)$$

where $O_{k,m} = l \cdot \int |\psi_k|^2 \cdot |\psi_m|^2 dz$ and $\Delta E_{km} = (|E_k - E_m| + \delta)/(l \cdot K)$, and are given in arbitrary units, while $\delta = 2$ meV is a tolerance factor.

Here, i and j represent the indexes of the injector states, L the left active region ground state, R the right active region upper laser state, l is the injector length, and K is the applied electric field. In the case of a five quantum well injector, calculations could be made up to $O^{(5)}$, but since the objective function O should only be a rough approximation of the electron cascade down the injector states, it is taken as

$$O = O^{(1)} + O^{(2)} + O^{(3)}. \quad (6)$$

In order to evaluate the expression (6), the wave functions of the entire structure have to be assigned to either an active region, a collector or an injector. This can be done by finding the wave functions of an isolated active region $\psi_i^{(A)}$, $i = 1, 2, 3$, and calculating their overlap $|\int \psi_i^{(A)} \psi_j dz|$ with each of the wave functions, ψ_j , $j = 1, \dots, 15$ of the full system. The three states with the largest overlap values are considered to originate from the active region. The rest are then separated into injector and collector wave functions by comparing the value of $z_j = \int \psi_j^2 \cdot z dz$ with the coordinate of the center of the active region z_A . If the value of z_j is less than z_A , they are regarded as injector wave functions.

Wave function classification is a more demanding task than it seems at first, since thin layers often result in wave functions that are not necessarily strictly spatially confined to

one region of the laser. This is especially noticeable in the case of the upper laser level and the ground injector level wave functions, which are sometimes hard to distinguish. Since this problem can lead to a completely incorrect evaluation of the target function, and hence an inappropriate injector design, it needs to be properly addressed. If any doubt about the origin of a wave function arises, the complete structure is recalculated in a very similar manner to the one performed for the active region, i.e., by finding the wave functions of an isolated injector region and calculating their overlap with the wave functions of a full system as well.

Naturally, the optimally designed injector must not have a significant influence on the active region energies and wave functions, so certain conditions need to be fulfilled. They regard the widths of the injector–active region barrier, which should be restricted to some minimal value (but must not be allowed to exceed the value given in Ref. 13 either), as well as the transition energy E_{12} , which can be allowed to vary only within the limits $33 \text{ meV} \leq E_{12} \leq 45 \text{ meV}$ in order to maintain the fast emptying of the lower laser level. In the case of a 4QW active region this condition is also extended to the value of E_{23} . Moreover, the matrix elements z_{12} and z_{23} , as well as z_{34} in the case of a 4QW active region, must not be reduced by more than 20% compared to the values obtained in the isolated active region.

The parameter vector consists of eleven layer thicknesses, all of which are varied independently. The optimization is performed for the external field value of $F = 48 \text{ kV/cm}$, while the barrier heights are set to 376 meV and are the same for all the barriers. Together with the active region optimization, this concludes the designing process.

B. The self-consistent model

In order to extract the output characteristics of the optimized structures, the energies and corresponding wave functions are re-evaluated using the transfer matrix method, and then a full self-consistent rate equation modeling of the electron transport is performed.^{24–27}

Consider a biased QCL structure with a large number of periods, each consisting of multiple quantum wells. The energy spectrum is formally continuous, but to a very good approximation can be considered to consist of quasidiscrete states (resonances). Based on the wave function localization properties, these states can be associated to different periods of the QCL, so that each period has an identical set of N states in the energy range of interest. Electron scattering occurs between states within the same period as well as between states associated to different periods, where the latter is clearly smaller for spatially more remote periods, because of the reduced wave function overlap. Assuming an identical electron distribution in each period, one may consider some “central” period with its P nearest neighbors on either side, and write the scattering rate equations in the steady-state

$$\sum_{j=1, j \neq i}^N n_j W_{j,i} - n_i \sum_{j=1, j \neq i}^N W_{i,j} + \sum_{k=1}^P \sum_{j=1, j \neq i}^N [n_j (W_{j,i+kN} + W_{j+kN,i}) - n_i (W_{i+kN,j} + W_{i,j+kN})] = 0, \quad (7)$$

where $i+kN$ is the i th state of the k th neighboring period,

$W_{i,j}$ is the total scattering rate from state i into state j and n_i is the electron concentration of the i th state. The first two sums in Eq. (7) are due to intraperiod while the third is a consequence of interperiod scattering. After finding the solution for electron densities n_i , macroscopic parameters of the system, like the current density and the modal gain, can be estimated. The scattering time $W_{i,j}$ is a function of both n_i and n_j —the initial and final subband populations, hence the set of equations needs to be solved self-consistently using an iterative procedure.

The current density can be calculated by subtracting the current density component which is the result of electrons scattering into the next periods of the QCL from the component caused by electrons scattering back. If we put a reference plane somewhere in the injection barrier of the central period, the current density flowing through that cross section can be written as

$$J = \sum_{k=1}^P \sum_{i=1}^N \sum_{j=1}^N k \cdot n_i (W_{i,j+kN} + W_{i+kN,j}) \quad (8)$$

The factor k in the summation, effective for non-nearest-neighbor scattering, originates from the scatterings from any QCL period left of the center period into any period right of it, or vice versa (i.e., skipping the central period, but passing through the reference plane). In order to reduce the number of scattering rate processes necessary to calculate the electron distribution and the corresponding current density [note that the number of total scattering rate processes equals to $N^2(2P+1)-N$], we introduce the “tight-binding” approximation assuming that only the nearest neighbors interact, and set $P=1$.

The choice of scattering mechanisms depends on the material and doping density, as well as on wavelength. For example, in the GaAs-based THz QCLs the energy separation between most of the subbands is smaller than the LO phonon energy and electron–electron scattering becomes an important scattering mechanism, hence necessitating a large number of possibly relevant scattering processes to be accounted for.²⁶

The modal gain is proportional to the population inversion Δn_{ij} , which can be obtained from the self-consistent solution under the steady-state condition:

$$G_M = \frac{4\pi e^2}{\epsilon_0 \underline{n}} \frac{\langle z_{ij} \rangle^2}{2\gamma_{ij} L_p \lambda} \Gamma \Delta n_{ij} \equiv g \Gamma J \quad (9)$$

where λ is the laser emission wavelength, $2\gamma_{ij}$ the experimental full width at half maximum of the electroluminescent spectrum below threshold, \underline{n} is the mode refractive index, ϵ_0 is the vacuum dielectric permittivity, L_p is the length of one period (active region+injector), Γ is the overlap factor between the optical mode and the core active region of the laser, and $\langle z_{ij} \rangle$ is the radiative transition matrix element.

Changing the bias field modifies the potential experienced by the electrons and consequently the energies and corresponding wave functions of the quasibound states. Hence, all the lifetimes and transition matrix elements change, influencing the electric current and, by modifying the subband populations, the gain. By repeating the self-

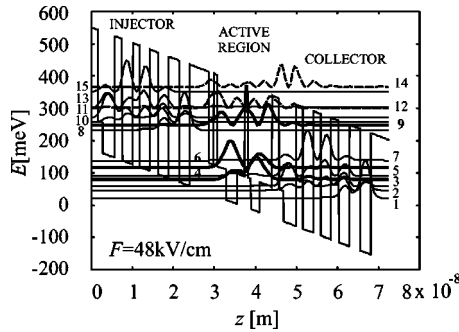


FIG. 2. A schematic diagram of quasibound energy levels and associated wave functions squared for one and a half periods of the optimized vertical transition (VT) steplike GaAs/Al_{0.11}Ga_{0.89}As/Al_{0.45}Ga_{0.55}As structure. The layer sequence of one period, in nanometers, starting from the injection barrier is: **4.6**, 1.2, **0.8**, 2.2, 2.6, 2.0, **0.7**, 0.7, 2.2, 3.0, **1.7**, 1.1, 3.0, **1.7**, 2.6, **1.8**, 2.4, **2.0**, 2.6, **2.6**, and 2.6. Normal scripts denote the wells, bold the barriers and underlined the steps, with the Al content of 11%. Both of the active region wave functions participating in the radiative transition (marked as levels 9 and 6) are mainly located in the central well, so the lasing transition taking place in this structure is evidently vertical by nature.

consistent procedure for a number of external fields, the total current density and corresponding modal gain can be calculated. The gain coefficient g can be estimated from the slope of the least square fit of the modal gain vs total current dependence $G_M(J)$, assuming its linearity.

III. NUMERICAL RESULTS AND DISCUSSION

The flexibility of the described method allows the design of devices operating in a wide range of wavelengths. In this work we address the optimization of the active and injector regions for a $\lambda \sim 9 \mu\text{m}$ operating QCL. This sets the transition energy to approximately 136 meV, while the energy difference between the ground and lower laser state (or three lower states in the case of 4QW) equals the LO phonon energy, i.e. 36 meV for GaAs structures. The optimization was carried out for the value of the applied field $F = 48 \text{ kV/cm}$, temperature $T = 300 \text{ K}$, and the sheet carrier density $N_s = 39 \times 10^{10} \text{ cm}^{-2}$, which was derived from the dopant profile per repeat period (and was initially, at the beginning of the self-consistent procedure, assumed to be distributed equally between the subbands of one period). As in the previously performed self-consistent analysis of mid-infrared QCL structures,²⁴ convergence was reached after 15 iterations. The results calculated for the optimized structures were then compared to those obtained for the previously realized structure with a triple-quantum well (TQW) active region, described in Ref. 13.

A schematic diagram of quasi-bound energy levels and associated wave functions squared for an injector-active region-injector section of the optimized vertical transition steplike GaAs/Al_{0.11}Ga_{0.89}As/Al_{0.45}Ga_{0.55}As structure is shown in Fig. 2. The layer sequence of one period, in nanometers, starting from the injection barrier is: **4.6**, 1.2, **0.8**, 2.2, 2.6, 2.0, **0.7**, 0.7, 2.2, 3.0, **1.7**, 1.1, 3.0, **1.7**, 2.6, **1.8**, 2.4, **2.0**, 2.6, **2.6**, and 2.6, where normal scripts represent the wells, bold the barriers and underlined the steps. According to the notation given in Ref. 24, the injector and collector regions are represented with five energy levels each, sub-

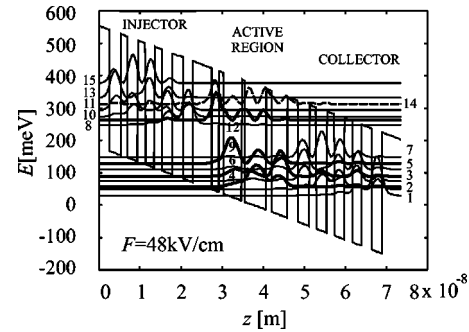


FIG. 3. One and a half period of the optimized double-LO phonon (2LO) GaAs/Al_{0.45}Ga_{0.55}As quantum cascade laser with a four quantum well active region (4QW). The layer sequence of one period, in nanometers, starting from the injection barrier is: **4.6**, 1.68, **1.12**, 4.48, **0.84**, 5.04, **1.4**, 3.83, **2.52**, 2.8, **1.7**, 2.52, **1.8**, 2.4, **2.0**, 2.24, **2.6** and 2.4, where normal scripts denote the wells and bold the barriers. The addition of an extra lower laser level enables a more efficient extraction mechanism into the injector region.

bands 1, 2, 3, 5, and 7 in the collector, and 8, 10, 11, 13, and 15 in the injector. Radiative transitions occur between the third and second state in the active region (levels 9 and 6), while level 4 is the active region ground state. The two additional levels (12 and 14) correspond to weakly-localized continuumlike transmission resonances. The Al content in the step equals 11%, which is approximately $\frac{1}{4}$ of the content in the barriers. The electron effective mass in the GaAs quantum wells was taken to be $0.067m_0$, while in the Al_{0.11}Ga_{0.89}As steps and Al_{0.45}Ga_{0.55}As barriers its value was $0.076m_0$ and $0.104m_0$, respectively. The energy gaps in the wells, steps and barriers were 1.426 eV, 1.566 eV, and 1.987 eV, while the height of the active region barriers was set to 376 meV. At the applied bias field of 48 kV/cm, for which the optimization was performed, the lasing wavelength amounts to $\lambda = 9.58 \mu\text{m}$. Due to the increased overlap between the lasing state wave functions, the optimized structure shows a significant increase of the dipole matrix element, $z_{96} = 2.84 \text{ nm}$.

The double LO-phonon structure (2LO) with the layer sequence of one period, in nanometers, starting from the injection barrier: **4.6**, 1.68, **1.12**, 4.48, **0.84**, 5.04, **1.4**, 3.83, **2.52**, 2.8, **1.7**, 2.52, **1.8**, 2.4, **2.0**, 2.24, **2.6**, 2.4 is shown in Fig. 3. The notation is the same as given for the vertical-transition structure, i.e. bold scripts represent the barriers and normal scripts the wells. The active region wave functions are denoted as 4, 6, 9 (the lower “ladder” states), 12 (upper laser state), and 14 (quasicontinuous state). For the optimization field value of 48 kV/cm we obtain the dipole matrix element $z_{96} = 2.75 \text{ nm}$ while the lasing wavelength amounts to $\lambda = 9.36 \mu\text{m}$. The active region itself consists of four quantum wells which result in only seven optimization parameters, all of them representing layer thicknesses. A remarkable decrease of the lower laser level population can be obtained by adding an extra level, forming a ladder of three states separated by optical phonon energy each, that will enable a more efficient extraction mechanism into the injector region.

A full self-consistent analysis for field values varying from 30 to 75 kV/cm and for temperatures of 77 K and 300 K was performed and the electric field-current density

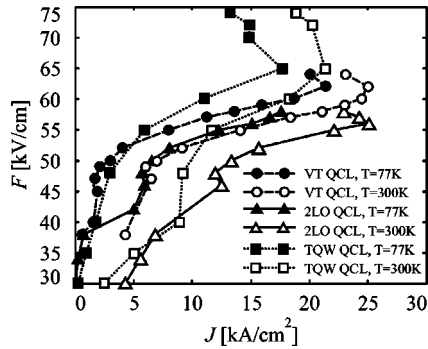


FIG. 4. Electric field vs current density characteristics at $T=77$ K and $T=300$ K in the optimized vertical transition (VT) steplike (dashed lines), double-LO phonon (2LO) 4QW (solid lines) and TQW QCL (Ref. 13) (dotted lines). The optimized vertical transition structure shows higher current densities in a wide range of applied fields.

characteristics for both optimized QCLs as well as the reference TQW laser¹³ are represented in Fig. 4. Good overall agreement with measurements in the reference TQW structure is found, with the calculated maximal current (before negative differential resistivity occurs) of ~ 17 kA/cm² being close to the measured ~ 20 kA/cm² at 77 K. It can be seen that the vertical transition structure demonstrates a considerable improvement in that higher current densities can be achieved with lower bias fields, thus potentially increasing the dynamical working range of the device.

Figure 5 shows the modal gain as a function of the current density, calculated with the parameter values $\mu=3.28$, $2\gamma_{96}=15$ meV (at $T=77$ K), $2\gamma_{96}=25$ meV (at $T=300$ K) and^{13,33} $\Gamma=0.31$. The period length of the vertical transition structure equals $L_p=44.3$ nm while in the case of the 2LO QCL it amounts to $L_p=45.9$ nm. In accordance with the experimentally obtained results, the mirror and waveguide losses are set to $\alpha_M+\alpha_W\approx 25$ cm⁻¹. From the intersection points of the total loss line and $G_M(J)$ lines we obtain threshold currents $J_{th}=4.5$ kA/cm² at 77 K, and $J_{th}=15$ kA/cm² at 300 K, for the TQW QCL, in a very good agreement with experiment ($J_{th}=3-4$ kA/cm² at 77 K and $J_{th}=15-17$ kA/cm² at 300 K).^{13,14} A good agreement with experimental results for the reference TQW structure indicates

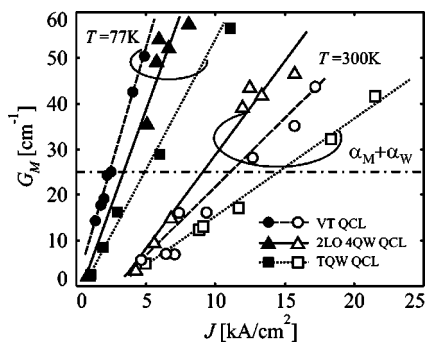


FIG. 5. Calculated modal gain dependence on the current density at 77 K and 300 K for the optimized vertical transition (VT) steplike (dashed lines), double-LO phonon (2LO) 4QW (solid lines) and TQW QCL (Ref. 13) (dotted lines). The symbols correspond to the calculated data, while the lines represent the least square fit which can be used to estimate the gain coefficient g . The threshold currents can be obtained from the intersection points with the total loss line $\alpha_M+\alpha_W\sim 25$ cm⁻¹.

the predicting capability of the suggested model. Besides a better inversion and a larger optical matrix element than in the conventional TQW design, a noticeable reduction of leakage from the injector into the lower laser level and an improved extraction from the ground active region level into the next injector (collector) are also predicted in the optimized structures, all of which result in smaller threshold (see Fig. 5) and larger saturation currents.

IV. SUMMARY

We have proposed a procedure for the design of globally optimal potential profile of a GaAs-based QCL with respect to its output characteristics. The technique has no restrictions regarding the number of the optimization parameters and demonstrates higher optimization capabilities compared to other techniques in use. The designs were evaluated by modeling of the carrier dynamics using the full self-consistent approach. While the gain and threshold currents calculated at 77 K and 300 K for the standard TQW active region structure show excellent agreement with experimental results, an improvement of these parameters is predicted for the optimized quantum cascade lasers. The described procedure is applicable to various active region and injector designs and could be used in further design work for other wavelength ranges.

ACKNOWLEDGMENTS

This work was supported by Royal Society (UK), the Ministry of Science (Serbia), and EPSRC (UK).

- ¹J. Faist, F. Capasso, D. L. Sivco, C. Sirtori, A. L. Hutchinson, and A. Y. Cho, *Science* **264**, 553 (1994).
- ²C. Gmachl, F. Capasso, D. L. Sivco, and A. Y. Cho, *Rep. Prog. Phys.* **64**, 1533 (2001).
- ³J. Faist, D. Hofstetter, M. Beck, T. Allen, M. Rochat, and S. Blaser, *IEEE J. Quantum Electron.* **38**, 533 (2002).
- ⁴F. Capasso, R. Paiella, R. Martini, R. Colombelli, C. Gmachl, T. L. Myers, M. S. Taubman, R. M. Williams, C. G. Bethea, K. Unterrainer, H. Y. Hwang, D. L. Sivco, A. Y. Cho, A. M. Sergent, H. C. Liu, and E. A. Whittaker, *IEEE J. Quantum Electron.* **38**, 511 (2002).
- ⁵C. Sirtori, P. Kruck, S. Barbieri, P. Collot, J. Nagle, M. Beck, J. Faist, and U. Oesterle, *Appl. Phys. Lett.* **73**, 3486 (1998).
- ⁶C. Sirtori, H. Page, and C. Becker, *Proc. R. Soc. London, Ser. A* **359**, 505 (2001).
- ⁷S.-C. Lee and A. Wacker, *Phys. Rev. B* **66**, 245314 (2002).
- ⁸C. Gmachl, D. L. Sivco, R. Colombelli, F. Capasso, and A. Y. Cho, *Nature (London)* **415**, 883 (2002).
- ⁹M. Beck, D. Hofstetter, T. Allen, J. Faist, U. Oesterle, M. Ilegems, E. Gini, and H. Melchior, *Science* **295**, 301 (2002).
- ¹⁰A. Evans, J. S. Yu, J. David, L. Doris, K. Mi, S. Slivken, and M. Razeghi, *Appl. Phys. Lett.* **84**, 314 (2004).
- ¹¹R. Kohler, A. Tredicucci, F. Beltram, H. E. Beer, E. H. Linfield, A. G. Davies, D. A. Ritchie, R. C. Iotti, and F. Rossi, *Nature (London)* **417**, 156 (2002).
- ¹²S. Kumar, B. S. Williams, S. Kohen, Q. Hu, and J. L. Reno, *Appl. Phys. Lett.* **84**, 2494 (2004).
- ¹³H. Page, C. Becker, A. Robertson, G. Glastre, V. Ortiz, and C. Sirtori, *Appl. Phys. Lett.* **78**, 3529 (2001).
- ¹⁴V. Ortiz, C. Becker, H. Page, and C. Sirtori, *J. Cryst. Growth* **251**, 401 (2003).
- ¹⁵H. Page, S. Dhillon, M. Calligaro, C. Becker, V. Ortiz, and C. Sirtori, *IEEE J. Quantum Electron.* **40**, 665 (2004).
- ¹⁶C. Pflügl, W. Schrenk, S. Andres, G. Strasser, C. Becker, C. Sirtori, Y. Bonetti, and A. Müller, *Appl. Phys. Lett.* **83**, 4698 (2003).
- ¹⁷S. Andres, W. Schrenk, E. Gornik, and G. Strasser, *Appl. Phys. Lett.* **80**,

- 1864 (2002).
- ¹⁸V. Spagnolo, G. Scamarcio, H. Page, and C. Sirtori, *Appl. Phys. Lett.* **84**, 3690 (2004).
- ¹⁹P. Harrison, D. Indjin, and R. W. Kelsall, *J. Appl. Phys.* **92**, 6921 (2002).
- ²⁰N. Imam, E. N. Glytsis, and T. K. Gaylord, *Superlattices Microstruct.* **30**, 29 (2001).
- ²¹J. Radovanović, V. Milanović, Z. Ikonić, and D. Indjin, *Semicond. Sci. Technol.* **17**, 716 (2002).
- ²²J. Radovanović, G. Todorović, V. Milanović, Z. Ikonić, and D. Indjin, *Phys. Rev. B* **63**, 115327 (1-9) (2001).
- ²³R. C. Iotti and F. Rossi, *Phys. Rev. Lett.* **87**, 146603 (2001).
- ²⁴D. Indjin, P. Harrison, R. W. Kelsall, and Z. Ikonić, *J. Appl. Phys.* **91**, 9019 (2002).
- ²⁵D. Indjin, P. Harrison, R. W. Kelsall, and Z. Ikonić, *Appl. Phys. Lett.* **81**, 400 (2002).
- ²⁶D. Indjin, P. Harrison, R. W. Kelsall, and Z. Ikonić, *IEEE Photonics Technol. Lett.* **15**, 15 (2003).
- ²⁷D. Indjin, P. Harrison, R. W. Kelsall, and Z. Ikonić, *Appl. Phys. Lett.* **82**, 1347 (2003).
- ²⁸P. Kruck, H. Page, C. Sirtori, S. Barbieri, M. Stellmacher, and J. Nagle, *Appl. Phys. Lett.* **76**, 3340 (2000).
- ²⁹B. Goffe, X. Ferrer, and X. Rogers, *J. Econometr.* **60**, 65 (1994).
- ³⁰<http://www.netlib.org/opt/simann.f>
- ³¹D. Indjin, S. Tomić, Z. Ikonić, P. Harrison, R. W. Kelsall, V. Milanović, and S. Kočinac, *Appl. Phys. Lett.* **81**, 2163 (2002).
- ³²S. Barbieri, C. Sirtori, H. Page, M. Beck, J. Faist, and J. Nagle, *IEEE J. Quantum Electron.* **36**, 736 (2000).
- ³³C. Sirtori, P. Kruck, S. Barbieri, H. Page, J. Nagle, M. Beck, J. Faist, and U. Oesterle, *Appl. Phys. Lett.* **75**, 3911 (1999).